

Engineering the grain boundary: a promising strategy to configure NiCoP₄O₁₂/NiCoP nanowire arrays for ultra-stable supercapacitor

Mengqi Cui¹, Zining Wang¹, Yuanye Jiang¹, Hui Wang (✉)^{1,2}

¹ State Key Laboratory Base for Eco-Chemical Engineering, College of Chemical Engineering, Qingdao University of Science and Technology, Qingdao 266042, China

² Guangdong Provincial Key Laboratory for Electronic Functional Materials and Devices, Huizhou University, Huizhou 516001, China

© Higher Education Press 2022

Abstract NiCoP₄O₁₂/NiCoP nanorod-like arrays with tunable grain boundary density and pores were synthesized by the processes composed of hydrothermal and pyrolysis, in which, the electron structure of Ni and Co atoms characterized by X-ray photoelectron spectroscopy was contemporaneous inverse manipulated. The optimized NiCoP₄O₁₂/NiCoP arrays have a high specific capacitance of 507.8 μAh · cm⁻² at 1 mA · cm⁻², and good rate ability of 64.7% retention at 30-folds increased current density. Importantly, an ultra-stable ability, 88.5% of retention after 10000 cycles, was achieved in an asymmetric cell assembled of the NiCoP₄O₁₂/NiCoP arrays with activated carbon. In addition, the energy and power densities of an asymmetric cell were higher than those of other work, demonstrating as-prepared NiCoP₄O₁₂/NiCoP arrays are promising electrodes for supercapacitors.

Keywords NiCo, array electrode, grain boundary, stability, supercapacitor

1 Introduction

Research in the field of electrochemical capacitor applications during the past twenty years showed that array-structured electrodes without binders exhibited better properties than conventional powder electrodes as a result of the relatively high conductivity due to the absence of non-conductive binder. These electrodes depicted higher energy storage capacity, and longer stable periods [1–4].

The electrochemical capacitance of the array-structured electrodes was majorly affected by the inherent interactions of the array components. Among the different metal elements with pseudocapacitive properties, Ni and Co compounds, including their (hydro) oxides, sulfides and phosphides, came into sharp focus due to their high theoretical capacitance. This was a result of the different valence transitions of Ni and Co atoms [5–7]. Compared to their (hydro) oxide, the sulfide and phosphide compounds of Ni and Co had relatively higher conductivity [8–11]. Recently, it has been demonstrated that the Ni and Co sulfides and phosphides transformed into (hydro) oxide as the process of charge storage caused by the redox reactions. Thus, Ni and Co heterostructures such as NiS/Ni₃S₂ [12], Ni₃S₂/CoNi₂S₄ [13], and Ni₃S₂@Co(OH)₂ [3] were formed on array electrodes. Synergy between these different components tuned the electronic structure of active sites and enhanced its intrinsic activity, resulting in higher pseudocapacitive performance than that of homostructures (single component). These facts suggested that the multicomponent Ni/Co-comprised array electrodes could be a prospective addition to the development of pseudocapacitors.

In addition to the intrinsic activity of the array electrodes, the physical structure of each component in the array was another determinant of its pseudocapacitive performance because of its relationship to the density of active sites [14,15]. Various strategies have been used by researchers to enhance such situations. Frequently, precise control of the component's morphological features, such as decreasing lamellar thickness of sheet-like primitives [16], and increasing density of sheet primitives [17], extending the length of wire primitives [18] as well as constructing a porous structure for primitives [10], etc. have been used to

expand the specific area to introduce more active sites in primitives. Among them, engineering rich grain-boundaries in the primitives proved to be an interesting strategy. Moreover, electron structures of grain-boundaries were also tuned to that of active sites in the plane; thus, enriching the activity of the array electrodes. In addition, the rich grain boundaries were combined with the porous structure to attune the density of active sites [19,20]. Therefore, developing rich grain-boundary arrays was another innovative avenue for improving an electrochemical capacitor.

In our previous work, a series of rich grain-boundaries materials have been synthesized and applied in the electrochemical field [21–23]. Particularly, the rich grain-boundaries array electrodes assembled using primitives such as Ni foam supported with Ni₃Se₂ nanowire [18] and Ni₂P nanosheet [24] exhibited good electrochemical performance owing to its abundant active sites. As demonstrated in our recent work and other related reports, the electrochemical activity of array electrodes were boosted by tuning their component. In the present work, array electrodes composed of bi-metal (Ni and Co) and binonmetal (O and P) primitives with rich grain-boundaries were fabricated, in which the density and electron structure of the active sites of the electrode primitives can be regulated by adjusting the portions of O and P. As expected, the electrode displayed good capacitor performance, particularly, better rate ability, owing to its unique structure.

2 Experimental

Preparation of the wire-like array electrode. Co(NO₃)₂ (8 mmol), Ni(NO₃)₂ (4 mmol) and urea (12 mmol) were dissolved in solution containing 30 mL of ethanol and 30 mL of water, followed by stirring at room temperature for 30 min. The solution obtained was transferred to a Teflon-lined autoclave, containing a piece of Ni foam (2 cm² × 3 cm²), and heated at 150 °C for 6 h. Subsequently, the Ni foam was rinsed with water and ethanol alternatively, and then tempered at 350 °C for 2 h to oxidize the Ni–Co layers formed on its surface. At the end of this process, NiCo₂O₄ electrode was obtained.

The NiCo₂O₄ electrode generated was phosphorized by introducing NaH₂PO₂ upstream in a tube furnace and annealed at 350 °C for 0, 5, 10, 20 and 30 min with a ramping of 5 °C·min⁻¹, respectively. The tube furnace was placed under a static N₂ atmosphere for 10 min before calcination. The resulting materials, differing only in phosphorization times, at 350 °C, were designated as NiCoP₄O₁₂/NiCoP-X (wherein, X = 0, 5, 10, 20, 30).

Physical characterization and electrochemical measurements were provided in Electronic Supplementary Material (ESM).

3 Results and discussion

The structural properties of the NiCoP₄O₁₂/NiCoP-10 sample generated were investigated by X-Rays Diffraction (XRD), Scanning Electron Microscope (SEM), and Transmission Electron Microscope (TEM), and the results are presented in Fig. 1. As shown in Fig. 1(a) of XRD patterns, signals from NiCoP₄O₁₂/NiCoP-10 sample were ascribed to the characteristic diffraction peaks of the four phases, (1) face-centered-cubic Ni phase derived from the Ni foam substrate, which was characterized by three strong peaks at $2\theta = 44.3^\circ$, 51.6° and 76.3° , (2) spinel NiCoP phase categorized by the clear peaks at $2\theta = 40.7^\circ$, 47.2° , and 54.2° corresponding to the (111), (210) and (300) planes, (3) NiCoP₄O₁₂ phase identified by the enlarged peaks at $2\theta = 21.0^\circ$, 23.5° , and 26.3° attributing to the (112), (021) and (221) planes, and (4) NiCo₂O₄ phase demonstrated by the weak peak at $2\theta = 36.1^\circ$, and diffraction peaks of the (311) planes, indicating that heterostructures of NiCoP₄O₁₂ and NiCoP (NiCoP₄O₁₂/NiCoP) were formed in the sample obtained. The micro-shape of the NiCoP₄O₁₂/NiCoP-10, generated by SEM, as observed in Fig. 1(b), was a uniform rod-like array, which was similar to that of the NiCo₂O₄ (Fig. S1, cf. ESM). Enlarged SEM images, presented in Fig. 1(c), displays the rods' tops overlap each other, indicating the formation of a bridged architecture. To further analyze the framework of the electrode, the fine structure of rods was investigated by TEM. As displayed in Fig. 1(d), the rod was composed of several irregular spherical particles, denoting the presence of multiple grain boundaries in the heterostructure. Magnified TEM in Fig. 1(e) showed many slit-like spaces between the particles, suggesting that NiCoP₄O₁₂/NiCoP-10 had not only a porous structure but also various void/solid interfaces. Explicit lattice fringes, having inter-planar distances of 0.24 and 0.22 nm, were clearly observed in Fig. 1(f), which were in accordance with the (311) plane of NiCo₂O₄ and (111) plane of NiCoP, respectively, which demonstrated the existence of two phases in the rods. Following the above results, the EDX spectrum of NiCoP₄O₁₂/NiCoP-10, as seen in Fig. 1(g), revealed the signals of Ni, Co, P, and O elements, implying that the rods were made of the four elements. In the selected region, presented as STEM in Fig. 1(h), the observed elemental mapping (Figs. 1(i–l)) depicted that the four elements were equally distributed throughout the rods.

The density of the grain boundary, an important factor of active sites, was assessed by grain size, which was tuned by adjusting the thermal-driven growth of NiCoP₄O₁₂ and NiCoP grains through different phosphating times at 350 °C. The SEM, TEM, XRD, grain size, and specific surface area of NiCoP₄O₁₂/NiCoP-X are shown in Fig. 2. As illustrated in Figs. 2(a–c), the samples obtained at 0, 5 and 20 min displayed rod-like appearances. When extending the time to 30 min, the size of rod primitives

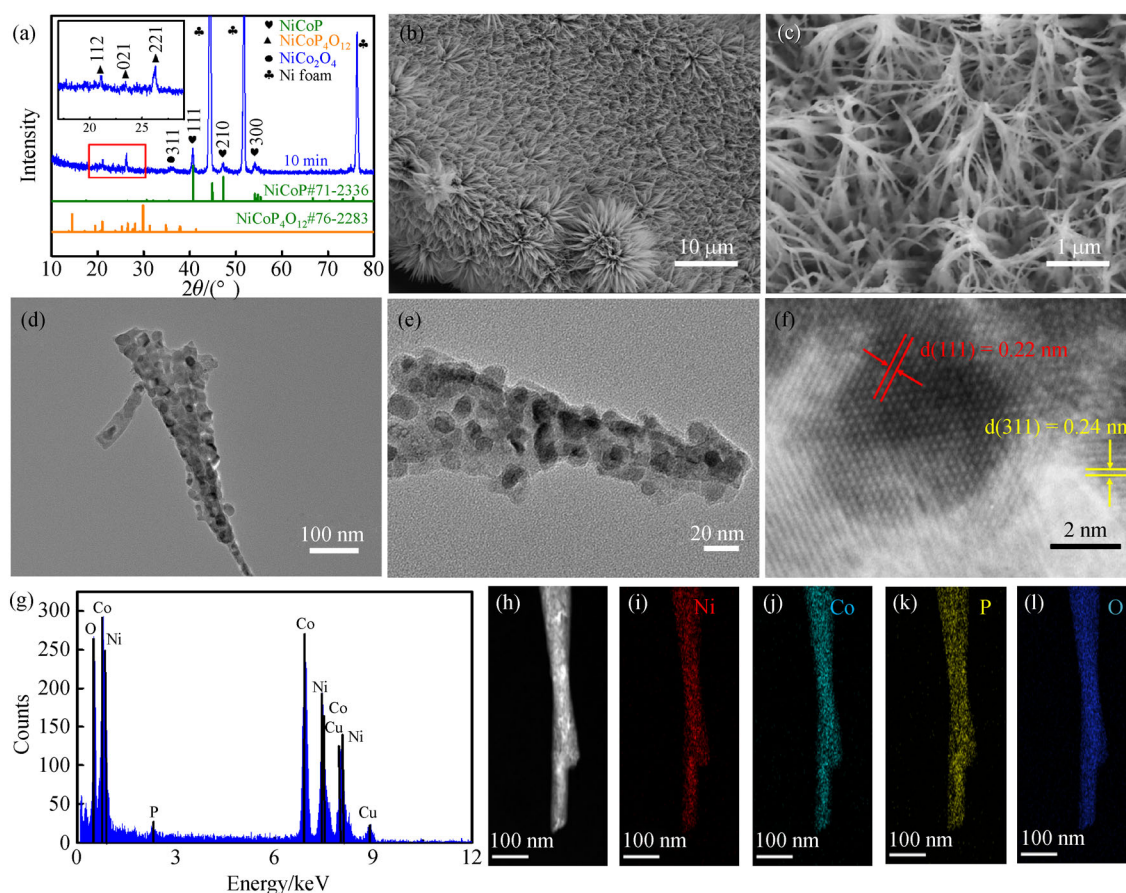


Fig. 1 (a) XRD pattern; (b, c) SEM images; (d–f) TEM images; (g) EDX; (h–l) STEM image and the element mapping of Ni, Co, P and O of NiCoP₄O₁₂/NiCoP-10.

become thick, although the shape of rod array is retained, as shown in Fig. S2 (cf. ESM), which is evident in the SEM image shown in Fig. S2(a). The deposit configuration of the grain was similar for NiCoP₄O₁₂/NiCoP-0 to NiCoP₄O₁₂/NiCoP-20, as observed from the TEM images depicted in Figs. 2(d–f). The small particle-assembled rods of NiCoP₄O₁₂/NiCoP-0 and NiCoP₄O₁₂/NiCoP-5 were similar to that of the NiCoP₄O₁₂/NiCoP-10 and NiCo₂O₄ (Fig. S1(c)). As the phosphating time increased, the particles visibly grew, as shown in the TEM image of NiCoP₄O₁₂/NiCoP-20 (Fig. 2(f)). However, this particle-accumulation structure disappeared in NiCoP₄O₁₂/NiCoP-30 sample due to the abnormal growth of grains as a result of long-term thermal treating (TEM image as observed in Fig. S2(b)). Thus, at 350 °C, a holding time of not more than 20 min was essential for retaining the feature of rich grain boundaries of samples.

The phase change of the bulk with phosphating time was also investigated using XRD. As depicted in Fig. 2(g), the relative intensity of (111) of NiCoP increased consistently from NiCoP₄O₁₂/NiCoP-0 to NiCoP₄O₁₂/NiCoP-30, while, the relative intensity of the NiCo₂O₄ diffraction peaks decreased with longer phosphating times. This indicated that a large number of NiCo oxides transformed

to NiCoP₄O₁₂ and NiCoP during phosphating. At the same time, it was also found that P atoms were progressively doped into the arrays, as perceived by the increased signals of P 2p in the X-ray photoelectron spectroscopy (XPS) survey spectrum as well as the negative shift of binding energy in the high-resolution P 2p XPS images of NiCoP₄O₁₂/NiCoP-0 to NiCoP₄O₁₂/NiCoP-30 (Fig. S3, cf. ESM). In addition, the complete absence of the feature of NiCoP₄O₁₂ signified that it had been converted to the NiCoP phase. From the above results, it was inferred that the NiCoP₄O₁₂/NiCoP-30 sample was composed of the single NiCoP.

In order to analyze the density of the grain boundary, the average crystalline size of the samples was calculated using the XRD patterns. However, the NiCoP₄O₁₂/NiCoP-30 sample was not considered because of the absence of granule-like features. As elucidated in Fig. 2(h), the average crystalline size of the samples increased with an increase in phosphating times, due to the growth of the grains by thermal treatment. The increase in the average crystalline size implied that the density of the grain boundary decreased from NiCo₂O₄ to NiCoP₄O₁₂/NiCoP-20.

The changes in the specific surface area of the samples

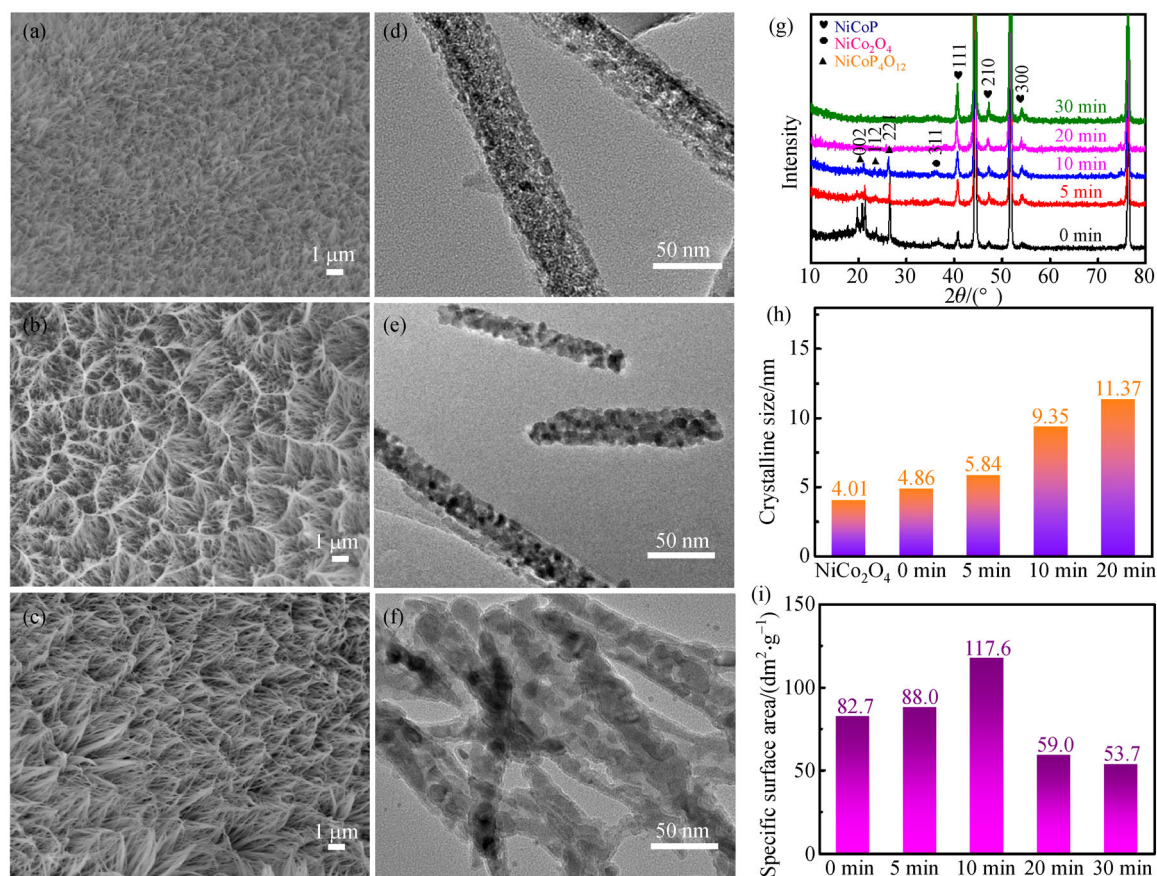


Fig. 2 (a) SEM, TEM patterns of the NiCoP₄O₁₂/NiCoP-X (X = 0 (a, d), 5 (b, e), 20 (c, f)) samples; (g) XRD patterns; (h) the average crystalline size; (i) specific surface area diagram of the NiCoP₄O₁₂/NiCoP-X samples indicated by the phosphating time.

caused by the varied phosphating times were investigated by Brunauer–Emmett–Teller (BET) method (Fig. S4, cf. ESM). From Fig. 2(i), the BET surface area increased gradually from NiCoP₄O₁₂/NiCoP-0 to NiCoP₄O₁₂/NiCoP-10 and reached its maximum at 117.6 dm²·g⁻¹. This phenomenon was ascribed to the following two reasons. On one hand, the growth of the grain leads to the increase of the specific surface area from NiCoP₄O₁₂/NiCoP-0 to NiCoP₄O₁₂/NiCoP-10 and decrease from NiCoP₄O₁₂/NiCoP-10 to NiCoP₄O₁₂/NiCoP-30. On the other hand, the pores among the particles would increase owing to the nanoscale Kirkendall effect from NiCoP₄O₁₂/NiCoP-0 to NiCoP₄O₁₂/NiCoP-30. Further, there was a balance between the two opposing factors, as a result of which the specific surface area reached its maximum value. All in all, the aforementioned results expounded that the density of the grain boundary and specific surface area of the samples can be tuned by varying the phosphating times.

Electrochemical properties of every NiCoP₄O₁₂/NiCoP-X sample, evaluated by cyclic voltammetry (CV) in 1 mol·L⁻¹ KOH alkaline electrolyte, are shown in Fig. 3. A couple of redox peaks, 0.43 V for positive scan and 0.25 V

for negative scan, appeared due to the redox transitions of Ni and Co, indicating the pseudocapacitive nature of the elements in alkaline electrolyte, as shown in Fig. 3(a). The current densities of the redox peaks increased at first, from NiCoP₄O₁₂/NiCoP-0 till NiCoP₄O₁₂/NiCoP-10, and then decreased for the NiCoP₄O₁₂/NiCoP-20 sample. Furthermore, the current density of the redox peaks of NiCoP₄O₁₂/NiCoP-10 was greater than that of NiCo₂O₄ and NiCoP (Fig. S5, cf. ESM), confirming that it was the best charge storage capability value. To further examine the charge storage mechanism of NiCoP₄O₁₂/NiCoP-10, CVs measurements for different scan rates (Fig. 3(b)) were calculated. The non-distortion CV curves at higher scan rates indicated faster electron transfer on the NiCoP₄O₁₂/NiCoP-10 electrode than at lower scan rates. The curve derived from Fig. 3(b) showed the power-law dependence of current on sweep rate and has been plotted in Fig. 3(c) based on the equation $i_p = av^b$, where i_p represented the peak current, a and b were the adjustable parameters, and v was the scan rate. The mechanisms of the charge storage of the electrodes were revealed by the slope of peak 1, denoting the parameter b . When the charge/discharge process was controlled by diffusion, b was 0.55; whereas b

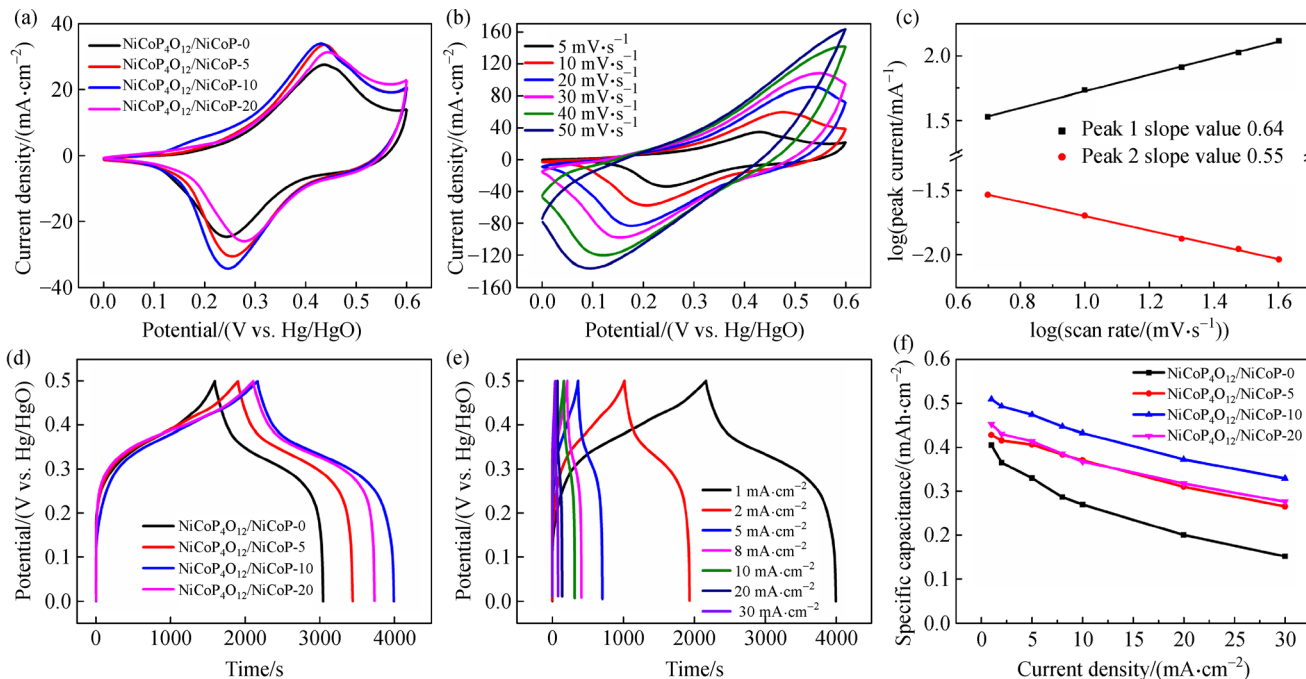


Fig. 3 (a) CV curves of all the NiCo₄O₁₂/NiCoP samples at 5 mV·s⁻¹; (b) CV curves of NiCo₄O₁₂/NiCoP-10 sample at various scan rates; (c) power law dependence of current on sweep rate; (d) galvanostatic charge-discharge (GCD) curves of all the NiCo₄O₁₂/NiCoP samples at 1 mA·cm⁻²; (e) GCD curves of NiCo₄O₁₂/NiCoP-10 at different current densities; (f) area specific capacitance vs. current density for all the NiCo₄O₁₂/NiCoP samples.

value of 0.64, as presented in Fig. 3(c), specified the mixed diffusion and surface-controlled electrochemical reactions occurring on the NiCo₄O₁₂/NiCoP-10 electrode.

GCD curves of every NiCo₄O₁₂/NiCoP-X electrode, depicted in Fig. 3(d), showed non-linear features. The potential plateaus existing between 0.35 and 0.48 V in GCD curves corresponded to the redox peaks of CV curves, indicating the battery-type behavior of electrodes during both charge and discharge processes [4,10]. The capacitance values of the samples were calculated based on their GCD curves, which were 403.6, 427.2, 507.8 and 451.1 μAh·cm⁻² from NiCo₄O₁₂/NiCoP-0 to NiCo₄O₁₂/NiCoP-20, respectively, with the current density of 1 mA·cm⁻². These values were higher than NiCo₂O₄ and NiCoP values (Fig. S5). Among the samples, NiCo₄O₁₂/NiCoP-10 had the highest capacitance, which was consistent with the CV results.

For studying the rate capability of the samples, a set of GCD measurements with different current densities were assessed. As depicted in Fig. 3(e), the time span decreased with the increase of current density from 1 to 30 mA·cm⁻² on the NiCo₄O₁₂/NiCoP-10 electrode, indicating that the capacitance of the sample dropped as a result of polarization on the electrode surface. At the current density of 30 mA·cm⁻², NiCo₄O₁₂/NiCoP-10's capacitance was 328.3 μAh·cm⁻², which was 64.7% lesser than the capacitance at the current density of 1 mA·cm⁻² (507.8 μAh·cm⁻²). Similarly, other samples also showed

higher loss of capacitance as NiCo₄O₁₂/NiCoP-10, which was shown in Fig. 3(f) and Fig. S6 (cf. ESM). Simultaneously, the cyclic stability of NiCo₂O₄ and NiCo₄O₁₂/NiCoP-X samples was analyzed using a three-electrode system, the result of which is shown in Fig. S7 (cf. ESM). Compared to other electrode samples, NiCo₄O₁₂/NiCoP-10 exhibited the best stability and lowest loss. After analyzing cyclic test results, we characterized the samples by TEM from the images displayed in Fig. S8 (cf. ESM). It was inferred that the grain boundaries sustained the morphology of the array electrode substantially after the stability test.

To reveal the principle of the good capacitive behavior of NiCo₄O₁₂/NiCoP-10, the process of electron and mass transfer was analyzed by electrochemical impedance spectroscopy (EIS) with the results shown in Fig. S9 (cf. ESM). The straight line at low frequency region and the semicircle at high frequency region indicate that charge storage process is controlled by the charge transport and mass transfer. Clearly, the slope of the straight line at low frequency for NiCo₄O₁₂/NiCoP-10 is larger than that of other frequency regions, suggesting the ion diffusion process in NiCo₄O₁₂/NiCoP-10 is easier than the bulk of the active mass, which is related to the richer porosity of NiCo₄O₁₂/NiCoP-10 than those of others supported by the specific surface areas obtained from BET. According to the fitting circuit diagram for the zoomed semicircle in Fig. S9(b), the charge transfer resistance (R_{ct}) were

estimated for the all electrode system. As listed Table S1 (cf. ESM), NiCoP₄O₁₂/NiCoP-10 has the smallest R_{ct} among all the samples, suggesting that the charge transfer resistance at electrode/electrolyte interface in NiCoP₄O₁₂/NiCoP-10 is smaller than others. This was attributed to its high electrical conductivity listed in Table S2 (cf. ESM) and high activity of Ni and Co sites due to their modified electron distribution, as depicted by the high-resolution 2p XPS of Co and Ni. Based on the EIS, we made equivalent electric circuits of samples, as shown in Fig. S9(c).

As presented in Fig. S10 (cf. ESM) and Table S3 (cf. ESM), the variation of binding energy of Ni 2p could be present from the peak of XPS spectra from NiCo₂O₄ to NiCoP₄O₁₂/NiCoP-30. As observed in the Ni 2p XPS of NiCo₂O₄, except for the two peaks coupled with satellites, two new peaks appeared at 851.3 and 868.6 eV in the Ni 2p spectra of the NiCoP₄O₁₂/NiCoP-X samples, which could be related to the two Ni⁰ peaks at the Ni 2p_{3/2} and Ni 2p_{1/2} electron orbits of formed NiCoP [25,26]. It is also noted that, the binding energy of the 2p_{3/2} peak of the NiCoP₄O₁₂/NiCoP-X samples (855.3 eV) is negative to that of the free Ni atom. As binding energies of reduced atoms shift negatively than free atoms, due to improved electronic shielding effect, some Ni atoms in the NiCoP₄O₁₂/NiCoP-X samples were in ‘reduced’ state [27,28] as the electrons were transferred from Co and P to Ni atoms, which was also proved by the change in the chemical state of Co atoms. There was an 11.6% increase in the portion of Co(III) increase from 52.0% in NiCoP₄O₁₂/NiCoP-0 to 63.6% in NiCoP₄O₁₂/NiCoP-30 (Fig. S11 (cf. ESM) and Table S4 (cf. ESM)). Moreover, the presence of “reduced-state” Ni species in NiCoP₄O₁₂/NiCoP-10 sample was larger than those in other samples, implying that the effect of electron reached the optimum. Thus, the NiCoP₄O₁₂/NiCoP-10 electrode had the highest capacity among all samples, proved by its porous framework and modified electron structure of Ni and Co atoms.

In order to analyze the capacitor performance of NiCoP₄O₁₂/NiCoP-10 electrode in practical applications, an assemble asymmetric supercapacitor (ASC) was assembled, using the sample as the cathode, activated carbon (AC) as the anode, and 1 mol·L⁻¹ KOH-solution as electrolyte. The performance test of the ASC is shown in Fig. 4. According to the CV curves of the assembled cell (Fig. 4(a)), it was observed that the anode exhibited an approximate rectangle shape, and the cathode displayed redox peaks, illustrating the ASC’s battery-like behavior. CV curves of ASC with different potential window ranges were recorded to choose the most appropriate range. The features depicted in Fig. 4(b), ascertained that rectangular CVs showed a wide range of redox currents. Polarization occurred in the sample as voltage of the ASC was increased to 1.7 V, therefore, 0–1.6 V of voltage window was determined to be suitable for the ASC.

The ability of charge transfer of the ASC was further investigated by CVs at various scan rates. As shown in Fig.

4(c), caused by the polarization, the CV’s rectangular shape is distorted with increasing scan rate. In more detail, at high scan rate, the adsorption/intercalation or desorption/deintercalation depth of OH⁻ ions into the electrode surface becomes lower owing to the inadequate time compared to that at low scan rate. Then, the faster the scan rate is, the more amplified the polarization will be, leading to a spindle-like shape in CVs at 100 mV·s⁻¹. It implies that the stored charge within the ASC decreases with the scan rate. To quantify the variation of the specific capacitor of the ASC, its GCD at various current densities were performed. As presented in Fig. 4(d), the non-standard straight line of all isosceles triangle curves indicates the supercapacitor typical for the ASC with the current density ranging from 2 to 30 mA·cm⁻². At 30 mA·cm⁻², the ASC’s specific capacitance drops to 377.5 μAh·cm⁻² corresponding to a 63.6% rate retention of its initial capacitance of 592.8 μAh·cm⁻² at 2 mA·cm⁻², indicating a good rate ability of the ACS.

Continuous GCD for 10000 cycles at 20 mA·cm⁻² was performed to test the long-term stability of the ASC. As shown in Fig. 4(e), the specific capacity of the ASC was 360 μAh·cm⁻² after 10000 cycles, with the loss of 0.0007% per cycle, indicating an outstanding cycling stability of ASC. Furthermore, the cycling stability of ASC was at the forefront of existing NiCo-based ASCs, as listed in Table S5 (cf. ESM). Meanwhile, ASC of the present study showed 370.3 and 30.2 W·kg⁻¹ power density at 38.3 and 1481.6 Wh·kg⁻¹ of energy density, respectively. The proposed ASC ranked foremost in reported NiCo-based ASCs, as plotted in Fig. 4(f). It can be seen from this figure that the performance of samples presented in the study was better than most nickel-cobalt-based compounds, which proves that the energy storage performance of our prepared samples is at the forefront. Similar to NiCo₂O₄/NiCoP, Ni–Co oxide showed 95.2 W·kg⁻¹ power density at 12 Wh·kg⁻¹ energy density. The performance of these samples was lower than the samples we prepared. These results explained that the as-prepared NiCoP₄O₁₂/NiCoP-10 electrode was a promising electrode in a practical ASC cell, which has been visualized in the pictures depicted in Fig. 4(g). The red LED light in series powered by the two ASCs could continuously work for longer than 12 min. Then we also conducted electrochemical measurement for AC anode and results were displayed in Fig. S12 (cf. ESM). Figure S12(a) is the CV curves at different scan rate; Fig. S12(b) shows its GCD curves at different current density; Fig. S12(c) is its specific capacity; and Fig. S12(d) is EIS images.

4 Conclusions

A series of rich-grain-boundary NiCoP₄O₁₂/NiCoP nanorods were easily grown on Ni foams by the two steps of hydrothermal and pyrolysis. The mechanism of porous

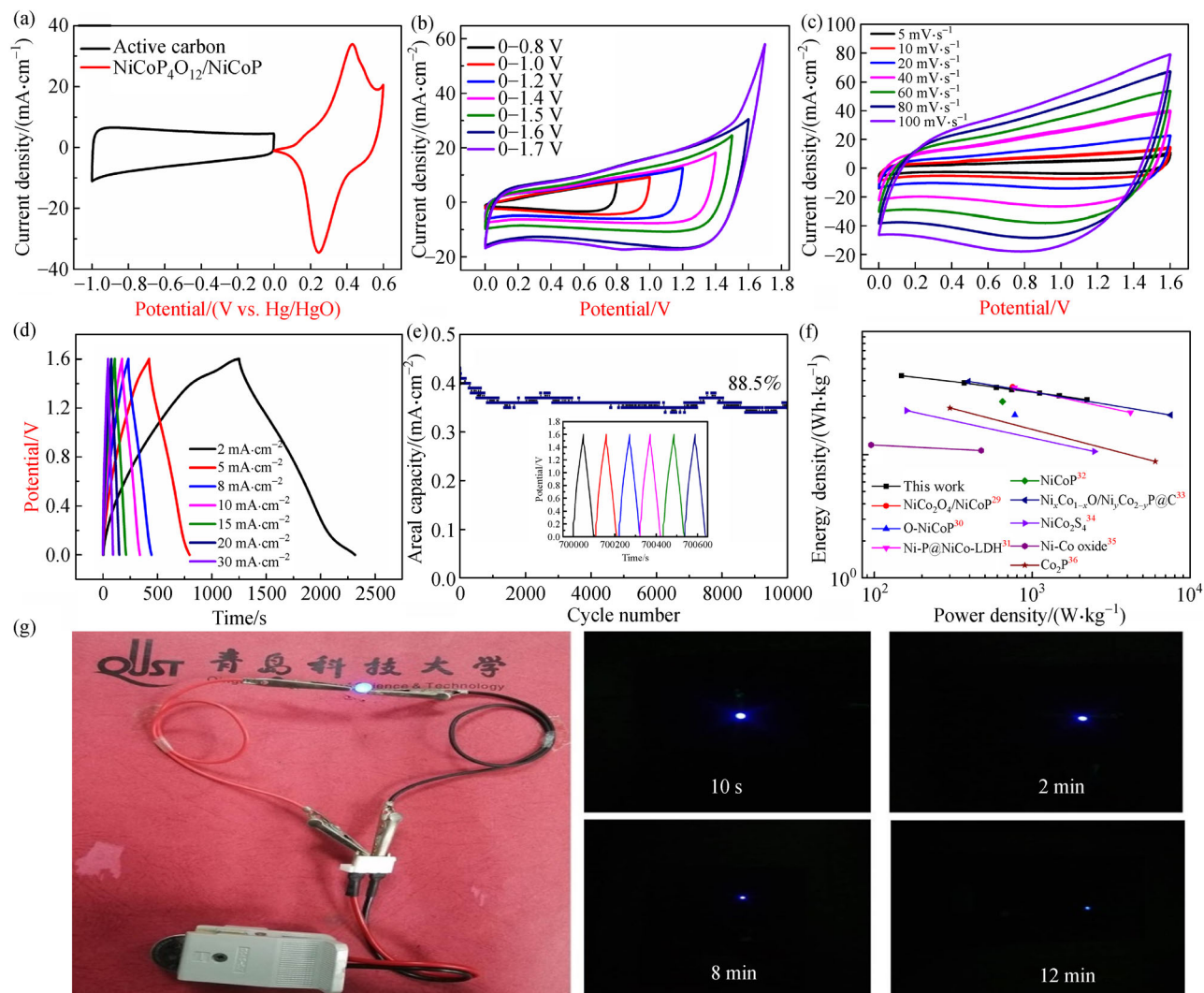


Fig. 4 (a) CV curves of activated carbon anode and NiCoP₄O₁₂/NiCoP-10; (b) CV curves of ASC measured at different operating voltages at 20 mV·s⁻¹; (c) CV curves of ASC at different scan rates from 10 to 100 mV·s⁻¹; (d) GCD curves of ASC at different current densities; (e) cycling stability of ASC at 20 mA·cm⁻²; (f) energy density vs. power density of NiCoP₄O₁₂/NiCoP-10//AC cell, compared with other studies; (g) red light-emitting diode (LED) powered by two series-connected coin cells after different illumination times.

structure and the grain boundary density of NiCoP₄O₁₂/NiCoP were revealed. The optimized NiCoP₄O₁₂/NiCoP-10 nanorods exhibited a high capacity of 507.8 μAh·cm⁻² at a current density of 1 mA·cm⁻² and good rate ability of a 64.7% retention with an increased 30-fold current density, as well as a high power density of 370.3 W·kg⁻¹ at an energy density of 38.3 Wh·kg⁻¹. Moreover, the ultra-stability of the NiCoP₄O₁₂/NiCoP-10 ASC is proved by only a 11.5% loss of the specific capacitor after 10000 cycles. The good capacitor behavior of NiCoP₄O₁₂/NiCoP-10 is ascribed to its porosity, rich grain boundary, and the electron effect owing to the electron transfer from Co and P to Ni. The results demonstrate significant potential and practical application of rich-grain-boundary NiCoP₄O₁₂/NiCoP nanorods in electrochemical energy storage devices.

Acknowledgements The authors thank the Natural Science Foundation of Shandong Province of China (Grant No. ZR2020MB024) and the Open Project Program of Guangdong Provincial Key Laboratory for Electronic Functional Materials and Devices, Huizhou University (Grant No. EFMD2021001Z) for financially supporting this work.

Electronic Supplementary Material Supplementary material is available in the online version of this article at <https://dx.doi.org/10.1007/s11705-021-2132-0> and is accessible for authorized users.

References

- Chen F, Ji S, Liu Q, Wang H, Liu H, Brett D J L, Wang G, Wang R. Rational design of hierarchically core-shell structured Ni₃S₂@Ni-MoO₄ nanowires for electrochemical energy storage. *Small*, 2018, 14(27): 1800791

- Cai D, Wang D, Liu B, Wang L, Liu Y, Li H, Wang Y, Li Q, Wang T. Three-dimensional $\text{Co}_3\text{O}_4@/\text{NiMoO}_4$ core/shell nanowire arrays on Ni foam for electrochemical energy storage. *ACS Applied Materials & Interfaces*, 2014, 6(7): 5050–5055
- Chen F, Wang H, Ji S, Linkov V, Wang R. Core-shell structured $\text{Ni}_3\text{S}_2@/\text{Co}(\text{OH})_2$ nano-wires grown on Ni foam as binder-free electrode for asymmetric supercapacitors. *Chemical Engineering Journal*, 2018, 345: 48–57
- Ji S, Ma Y, Wang H, Key J, Brett D J L, Wang R. Cage-like $\text{MnO}_2\text{-Mn}_2\text{O}_3$ hollow spheres with high specific capacitance and high rate capability as supercapacitor material. *Electrochimica Acta*, 2016, 219: 540–546
- Lu Z, Yang Q, Zhu W, Chang Z, Liu J, Sun X, Evans D G, Duan X. Hierarchical $\text{Co}_3\text{O}_4@/\text{Ni-Co-O}$ supercapacitor electrodes with ultrahigh specific capacitance per area. *Nano Research*, 2012, 5(5): 369–378
- Chen G, Liaw S S, Li B, Xu Y, Dunwell M, Deng S, Fan H, Luo H. Microwave-assisted synthesis of hybrid $\text{Co}_x\text{Ni}_{1-x}(\text{OH})_2$ nanosheets: Tuning the composition for high performance supercapacitor. *Journal of Power Sources*, 2014, 251: 338–343
- Chen H, Hu L, Yan Y, Che R, Chen M, Wu L. One-step fabrication of ultrathin porous nickel hydroxide-manganese dioxide hybrid nanosheets for supercapacitor electrodes with excellent capacitive performance. *Advanced Energy Materials*, 2013, 3(12): 1636–1646
- Liu Y, Liu G, Nie X, Pan A, Liang S, Zhu T. In situ formation of $\text{Ni}_3\text{S}_2\text{-Cu}_{1.8}\text{S}$ nanosheets to promote hybrid supercapacitor performance. *Journal of Materials Chemistry. A, Materials for Energy and Sustainability*, 2019, 7(18): 11044–11052
- Wang Z, Chen F, Kannan P, Ji S, Wang H. Nickel phosphate nanowires directly grown on Ni foam as binder-free electrode for pseudocapacitors. *Materials Letters*, 2019, 257: 126743
- Wang Z, Wang H, Ji S, Wang X, Zhou P, Huo S, Linkov V, Wang R. Hollow-structured NiCoP nanorods as high-performance electrodes for asymmetric supercapacitors. *Materials & Design*, 2020, 193: 108807
- Wang Z, Wang H, Ji S, Wang H, Brett D J L, Wang R. Design and synthesis of tremella-like Ni-Co-S flakes on co-coated cotton textile as high-performance electrode for flexible supercapacitor. *Journal of Alloys and Compounds*, 2020, 814: 151789
- Chen F, Wang H, Ji S, Linkov V, Wang R. High-performance all-solid-state asymmetric supercapacitors based on sponge-like $\text{NiS/Ni}_3\text{S}_2$ hybrid nanosheets. *Materials Today. Energy*, 2019, 11: 211–217
- Chen F, Wang H, Ji S, Linkov V, Wang R. A 3D petal-like $\text{Ni}_3\text{S}_2/\text{CoNi}_2\text{S}_4$ hybrid grown on Ni foam as a binder-free electrode for energy storage. *Sustainable Energy & Fuels*, 2018, 2(8): 1791–1798
- Chen S, Xing W, Duan J, Hu X, Qiao S Z. Nanostructured morphology control for efficient supercapacitor electrodes. *Journal of Materials Chemistry. A, Materials for Energy and Sustainability*, 2013, 1(9): 2941–2954
- Liu X Y, Zhang Y Q, Xia X H, Shi S J, Lu Y, Wang X L, Gu C D, Tu J P. Self-assembled porous NiCo_2O_4 hetero-structure array for electrochemical capacitor. *Journal of Power Sources*, 2013, 239: 157–163
- Zhang L, Wang H, Ji S, Wang X, Wang R. Porous-sheet-assembled $\text{Ni}(\text{OH})_2/\text{NiS}$ arrays with vertical in-plane edge structure for supercapacitors with high stability. *Dalton Transactions (Cambridge, England)*, 2019, 48(46): 17364–17370
- Wang Z N, Ji S, Liu F S, Wang H, Wang X Y, Wang Q Z, Pollet B G, Wang R F. Highly efficient and stable catalyst based on $\text{Co}(\text{OH})_2@/\text{Ni}$ electroplated on Cu-metallized cotton textile for water splitting. *ACS Applied Materials & Interfaces*, 2019, 11(33): 29791–29798
- Shi X, Wang H, Kannan P, Ding J, Ji S, Liu F, Gai H, Wang R. Rich-grain-boundary of Ni_3Se_2 nanowire arrays as multifunctional electrode for electrochemical energy storage and conversion applications. *Journal of Materials Chemistry. A, Materials for Energy and Sustainability*, 2019, 7(7): 3344–3352
- Thongsamrit W, Phrompet C, Maneesai K, Karaphun A, Tuichai W, Sriwong C, Ruttanapun C. Effect of grain boundary interfaces on electrochemical and thermoelectric properties of a $\text{Bi}_2\text{Te}_3/\text{reduced graphene oxide}$ composites. *Materials Chemistry and Physics*, 2020, 250(1): 123196
- Yuan C, Li J, Hou L, Lin J, Zhang X, Xiong S. Polymer-assisted synthesis of a 3D hierarchical porous network-like spinel NiCo_2O_4 framework towards high-performance electrochemical capacitors. *Journal of Materials Chemistry. A, Materials for Energy and Sustainability*, 2013, 1(37): 11145
- Wang H, Liu Z, Ma Y, Julian K, Ji S, Linkov V, Wang R. Synthesis of carbon-supported PdSn-SnO_2 nanoparticles with different degrees of interfacial contact and enhanced catalytic activities for formic acid oxidation. *Physical Chemistry Chemical Physics*, 2013, 15(33): 13999–14005
- Ma Y, Wang R, Wang H, Linkov V, Ji S. Evolution of nanoscale amorphous, crystalline and phase-segregated PtNiP nanoparticles and their electrocatalytic effect on methanol oxidation reaction. *Physical Chemistry Chemical Physics*, 2014, 16(8): 3593–3602
- Ma Y, Wang H, Lv W, Ji S, Pollet B G, Li S, Wang R. Amorphous PtNiP particle networks of different particle sizes for the electro-oxidation of hydrazine. *RSC Advances*, 2015, 5(84): 68655–68661
- Wu Y T, Wang H, Ji S, Pollet B G, Wang X Y, Wang R F. Engineered porous Ni_2P -nanoparticle/ Ni_2P -nanosheet arrays via the Kirkendall effect and Ostwald ripening towards efficient overall water splitting. *Nano Research*, 2020, 13(8): 2098–2105
- Moulder J F, Stickle W F, Sobol P C, Bomben K D. *Handbook of X-Ray Photoelectron Spectroscopy*. 2nd ed. Waltham: Perkin-Elmer Corporation, 1992, 1–262
- Shi X, Key J, Ji S, Linkov V, Liu F, Wang H, Gai H, Wang R. Ni $(\text{OH})_2$ nanoflakes supported on 3D Ni_3Se_2 nanowire array as highly efficient electrodes for asymmetric supercapacitor and Ni/MH battery. *Small*, 2019, 15(29): 1802861
- Sakamoto K, Hayashi F, Sato K, Hirano M, Ohtsu N. XPS spectral analysis for a multiple oxide comprising NiO, TiO_2 , and NiTiO_3 . *Applied Surface Science*, 2020, 526: 146729
- Bondarchuk O, LaGrow A P, Kvasha A, Thieu T, Ayerbe E, Urdampilleta I. On the X-ray photoelectron spectroscopy analysis of $\text{LiNi}_x\text{Mn}_y\text{Co}_z\text{O}_2$ material and electrodes. *Applied Surface Science*, 2021, 535: 147699
- Zong Q, Yang H, Wang Q, Zhang Q, Xu J, Zhu Y, Wang H, Wang H, Zhang F, Shen Q. $\text{NiCo}_2\text{O}_4/\text{NiCoP}$ nanoflake-nanowire arrays: a homogeneous hetero-structure for high performance asymmetric hybrid supercapacitors. *Dalton Transactions (Cambridge, England)*,

- 2018, 47(45): 16320–16328
30. Zhang Y, Sun L, Zhang L, Li X, Gu J, Si H, Wu L, Shi Y, Sun C, Zhang Y. Highly porous oxygen-doped NiCoP immobilized in reduced graphene oxide for supercapacitive energy storage. *Composites. Part B, Engineering*, 2020, 182: 107611
 31. Xing J, Du J, Zhang X, Shao Y, Zhang T, Xu C A. Ni-P@NiCo LDH core-shell nanorod-decorated nickel foam with enhanced areal specific capacitance for high-performance supercapacitors. *Dalton Transactions (Cambridge, England)*, 2017, 46(30): 10064–10072
 32. Lan Y, Zhao H, Zong Y, Li X, Sun Y, Feng J, Wang Y, Zheng X, Du Y. Phosphorization boosts the capacitance of mixed metal nanosheet arrays for high performance supercapacitor electrodes. *Nanoscale*, 2018, 10(25): 11775–11781
 33. Shao Y, Zhao Y, Li H, Xu C. Three-dimensional hierarchical $\text{Ni}_x\text{Co}_{1-x}\text{O}/\text{Ni}_y\text{Co}_{2-y}\text{P}@C$ hybrids on nickel foam for excellent supercapacitors. *ACS Applied Materials & Interfaces*, 2016, 8(51): 35368–35376
 34. Kong W, Lu C, Zhang W, Pu J, Wang Z. Homogeneous core-shell NiCo_2S_4 nanostructures supported on nickel foam for supercapacitors. *Journal of Materials Chemistry. A, Materials for Energy and Sustainability*, 2015, 3(23): 12452–12460
 35. Tang C, Tang Z, Gong H. Hierarchically porous Ni-Co oxide for high reversibility asymmetric full-cell supercapacitors. *Journal of the Electrochemical Society*, 2012, 159(5): A651–A656
 36. Chen X, Cheng M, Chen D, Wang R. Shape-controlled synthesis of Co_2P nanostructures and their application in supercapacitors. *ACS Applied Materials & Interfaces*, 2016, 8(6): 3892–3900